J Nanopart Res (2018) 20:57
https://doi.org/10.1007/s11051-018-4157-y

RESEARCH PAPER

Theranostic nanoplatform based on polypyrrole nanoparticles for photoacoustic imaging and photothermal therapy

Hui Liu · Wenchao Li · Yang Cao · Yuan Guo · Yuejun Kang

Received: 26 September 2017 / Accepted: 8 February 2018

Abstract Development of effective theranostic nanoplatforms against malignant tumor is still a challenge. With desirable near-infrared (NIR) light-responsive properties, polypyrrole nanoparticles (PPy NPs) are one of the promising theranostic candidates for cancer photoacoustic imaging and photothermal therapy. Here, PPy NPs with distinct sizes were prepared using a facile aqueous dispersion polymerization method. The formed PPy NPs are uniform in size with narrow size distribution. Characterization data show that PPy NPs with a diameter around 50 nm (P50) display stronger absorption in the NIR range compared to 40 and 60 nm PPy NPs, which further influences their photo-responsive properties. Due to their higher NIR absorption, P50 NPs have better photoacoustic imaging property and photothermal conversion ability than the other two kinds of PPy NPs. The photothermal stability of P50 NPs was proved to be excellent. The CCK-8 assays show that PPy NPs have obvious acute cytotoxicity within 6 h and desirable cytocompatibility for longer incubation time (12 and 24 h). After 6-h incubation, P50 NPs could be internalized by HeLa cells. Their photothermal tumor ablation effect was demonstrated under 808-nm laser irradiation. These findings may provide in-depth understanding of the PPy-based multifunctional nanomaterials for the development of theranostic systems against cancer.

Keywords Theranostic nanoplatform · Polypyrrole nanoparticles · Photoacoustic imaging · Photothermal therapy · Nanomedicine

H. Liu (✉) · W. Li · Y. Kang (✉)
Institute for Clean Energy and Advanced Materials, Faculty of Materials and Energy, Southwest University, Chongqing 400715, China
e-mail: liuhui2016@swu.edu.cne-mail: yjkang@swu.edu.cn

H. Liu · W. Li · Y. Kang
Chongqing Engineering Research Center for Micro-Nano Biomedical Materials and Devices, Chongqing 400715, China

H. Liu
State Key Laboratory of Molecular Engineering of Polymers, Fudan University, Shanghai 200433, China

Y. Cao · Y. Guo
Chongqing Key Laboratory of Ultrasound Molecular Imaging, Institute of Ultrasound Imaging, Second Affiliated Hospital, Chongqing Medical University, Chongqing 400010, China

Introduction

Developing desirable theranostic nanoplatforms against cancer is still a huge challenge and has attracted increasing attention (Deng et al. 2015; Opoku-Damoah et al. 2016). By integrating diagnostic and therapeutic functions, the resulting theranostic nanoplatforms can precisely analyze disease status, and their metabolism and therapeutic effect can be monitored in real time (Li et al. 2017). Selection of suitable imaging agents and therapeutic agents for integration with the nanoplatform is of great significance, which needs to be designed carefully.

The conventional imaging technologies have been well developed and contributed significantly to various diagnostic applications in clinics. For example, X-ray

Published online: 27 February 2018

computed tomography (CT) and magnetic resonance (MR) imaging are popular noninvasive imaging techniques and can provide diagnostic information with high spatial resolution. However, the inherent limitations of each single imaging modality have restricted them from satisfying the increasing practical demands (Huang et al. 2012; Liao et al. 2014). It is a pressing demand to develop multimodal imaging technologies. Particularly, hybrid nanoplatforms comprising two or more imaging elements are developed to realize multimodal imaging (Liu et al. 2015). For example, combination of gold and iron or gadolinium could realize CT/MR dual-mode imaging (Cai et al. 2012; Wen et al. 2013). However, this multimodal imaging method may complicate the probe preparation and imaging processes. Photoacoustic (PA) imaging is a recently developed noninvasive imaging modality that combines the high resolution of ultrasound detection and high sensitivity of optical imaging (Hu et al. 2016b; Zha et al. 2013a). PA imaging has shown a promising potential for brain imaging (Wang et al. 2003), lymph node imaging (Song et al. 2008), and tumor diagnosis (Fan et al. 2015; Zhang et al. 2016).

The contrast agents that are responsive to near-infrared (NIR) light for PA imaging could also transfer the absorbed optical energy into heat for photothermal therapy (PTT) applications (Guha et al. 2016; Huang et al. 2013). PTT is a noninvasive and effective cancer therapy method (Wang et al. 2014a; Wang et al. 2015). Compared to traditional therapeutic methods, PTT is featured by tissue specificity and minimal side effect, therefore attracting more attention (Ahmad et al. 2016; Song et al. 2015). To date, several nanoplatforms with desirable NIR light absorption and transformation properties have been developed as PA imaging/PTT theranostic nanoplatforms, such as metal-based nanostructures (Chen et al. 2014b; Cheng et al. 2014; Song et al. 2014; Wang et al. 2017; Zha et al. 2013c), carbon-based nanomaterials (Chen et al. 2014a; Yang et al. 2013), and polymer nanoparticles (NPs) (Chen et al. 2012; Hu et al. 2016a; Liang et al. 2017). Among them, polypyrrole (PPy) NPs are a kind of promising candidates attributed to their convenient and controllable synthesis, and desirable photo-responsive properties (Jin et al. 2014; Liang et al. 2015). They have proved biocompatibility with minimal long-term cytotoxicity in low concentration range (Zha et al. 2013b). Previous studies showed that the size of PPy NPs could affect their photothermal properties (Wang et al. 2014b). However, the size range investigated previously is limited and the size effect on their photoacoustic properties is still unclear. In addition, the cytotoxicity of PPy NPs needs to be evaluated systematically.

In this work, PPy NPs were prepared through a facile one-step aqueous dispersion polymerization method using polyvinyl alcohol (PVA) as a stabilizer and $FeCl_3$ as an oxidant. By regulating the PVA concentration, the NP sizes can be tuned precisely. The size, morphology, optical properties, and photothermal stabilities of the formed PPy NPs were characterized, and the size effect on their photoacoustic and photothermal properties was investigated in detail. HeLa cells were selected as the cancer cell model in vitro to study the cytocompatibility and the photothermal ablation capability of the PPy NPs.

Experimental section

Materials

Pyrrole (98%), iron(III) chloride hexahydrate ($FeCl_3 \cdot 6H_2O$, 97%), and dopamine hydrochloride were purchased from J&K. Poly(vinyl alcohol) (Mw 9–10 k, 80% hydrolyzed) was obtained from Aldrich. 5-Carboxy fluorescein-NHS (5-FAM-NHS) was provided by Xi'an Ruixi Biological Technology Co., Ltd. Hoechst 33342 was obtained from Beyotime. All the chemicals were used without further purification. Deionized (DI) water (18.2 MΩ cm) from a water purification system (Synergy, Millipore) was used in all the preparation process.

Preparation of polypyrrole nanoparticles

Polypyrrole nanoparticles were synthesized according to a method reported in the literature with some modifications (Hong et al. 2010). In a typical procedure for 50 nm PPy (P50) NPs, PVA (305.0 mg, final concentration at 37 mg/mL) was firstly dissolved using DI water and then $FeCl_3 \cdot 6H_2O$ (514.8 mg) was added and mixed for 1 h. Then the mixture was transferred into ice-water bath and 57.2 μL of pyrrole monomer (with $FeCl_3 \cdot 6H_2O$:pyrrole ratio at 9 mg:1 μL) was added. The oxidation polymerization reaction was carried out in ice-water bath for 4 h. For preparation of 40 and 60 nm PPy (P40 and P60) NPs, the concentration of PVA was adjusted to 80 and 12 mg/mL, respectively. The formed PPy NPs were collected by centrifugation and washed with DI water.

Characterization of PPy NPs

The size and morphology of the formed PPy NPs were determined by a field emission scanning electron microscope (FE-SEM, JSM-7800F). Their UV-vis absorption spectra were measured on a UV spectrophotometer (UV-1800, Shimadzu). The hydrodynamic size and surface potential of the PPy NPs were measured by dynamic light scattering (DLS, Nano ZS90, Malvern). Taking P50 NPs for example, after being dispersed in different kinds of solvents, such as water, water plus 10% fetal bovine serum (FBS), pH 6.5 buffer (similar to the pH value of tumor microenvironment), and pH 7.4 buffer (similar to the pH value of normal physiological environment), their hydrodynamic sizes, polydispersities, and zeta potentials were measured by dynamic light scattering.

Photoacoustic performance evaluation

A small animal PA imaging equipment (Vevo LAZR, Canada) was used to evaluate the photoacoustic properties of PPy NPs with distinct sizes. This apparatus was equipped with a laser emission probe (wavelength range: 680–970 nm), a diagnostic US probe, and a computer processing system. The experiment was carried out using agarose gel molds with a hole of 2 cm in depth and 0.5 cm in diameter. The aqueous solutions of PPy NPs were injected into the hole for test. The PA images were acquired with the depth of 20.00 mm and width of 23.04 mm under laser wavelength of 704 nm. The PA signals were averaged within a circle of around 5 mm^2.

Photothermal performance evaluation

PPy NPs with the same concentration but different sizes were suspended in aqueous solution and treated with an 808-nm NIR laser (LWIRL808, LASERWAVE) at a power density of 1.0 W/cm^2. The temperature changes were recorded at certain time intervals. Then, P50 NP aqueous solutions of series concentrations were irradiated using the same laser to study the concentration-dependent photothermal property. The photothermal reproducibility and stability were evaluated by treating P50 NP solution of 20 ppm using 5 cycles of heating (10 min)-cooling (20 min) process. DI water without NPs was tested as a blank control. After 5 cycles, the P50 NPs were characterized and compared with the NPs before laser irradiation.

In vitro cytotoxicity assay and intracellular localization study

HeLa cells (a human cervical carcinoma cell line) and L929 cells (a mouse fibroblast cell line) were purchased from Cell Bank, Chinese Academy of Sciences, and cultured using MEM medium supplemented with 10% fetal bovine serum and 1% penicillin-streptomycin at 37 °C and 5% CO_2.

A CCK-8 colorimetric assay was used to quantify the viability of cells treated with P50 NPs of different concentrations. Briefly, 1.0×10^4 cells per well were seeded into a 96-well plate. After 1 day, the medium was replaced with fresh medium containing P50 NPs of different concentrations. Cells treated with PBS buffer were also tested as a blank control. Besides 24 h, incubation times of 2, 6, and 12 h were also tested to study the acute cytotoxicity of P50 NPs. After incubation, the medium were removed and each well was washed using PBS buffer. Then 100 μL of CCK-8 solutions was added and the cells were incubated for additional 0.5 h under normal culture condition. Then, the absorbance of each well was recorded at 450 nm using a microplate reader (SPARK 10 M, Tecan). For each sample, mean and standard deviation for the triplicate wells were reported. After treatment with P50 NPs of different concentrations for 24 h, cell morphologies were observed using an inverted microscope (IX73, Olympus).

Then, the cellular uptake and localization of P50 NPs was studied. Firstly, the surface of P50 NPs was activated using the polydopamine coating method (Yang et al. 2017). Then the NPs were fluorescence-labeled by 5-FAM through the chemical connection of NHS on 5-FAM and the amino groups on polydopamine. One hundred parts per million of the modified NPs was incubated with HeLa cells for 6 h. Then, free NPs were removed and the cells were washed using PBS buffer three times. The cell nuclei were stained using Hoechst 33342. After that, the cells were observed using a confocal laser scanning microscopy (LSM 780, Carl Zeiss, Germany).

In vitro photothermal therapy of cancer cells

To study the photothermal effect of PPy NPs on cell viability, 1.0×10^4 HeLa cells in a 96-well plate were co-incubated with P50 NPs of different concentrations for 12 h. Then, the medium containing nanoparticles was removed. Each well was irradiated by an 808-nm laser at a power density of 1.0 W/cm^2 for 5 or 10 min. The cell

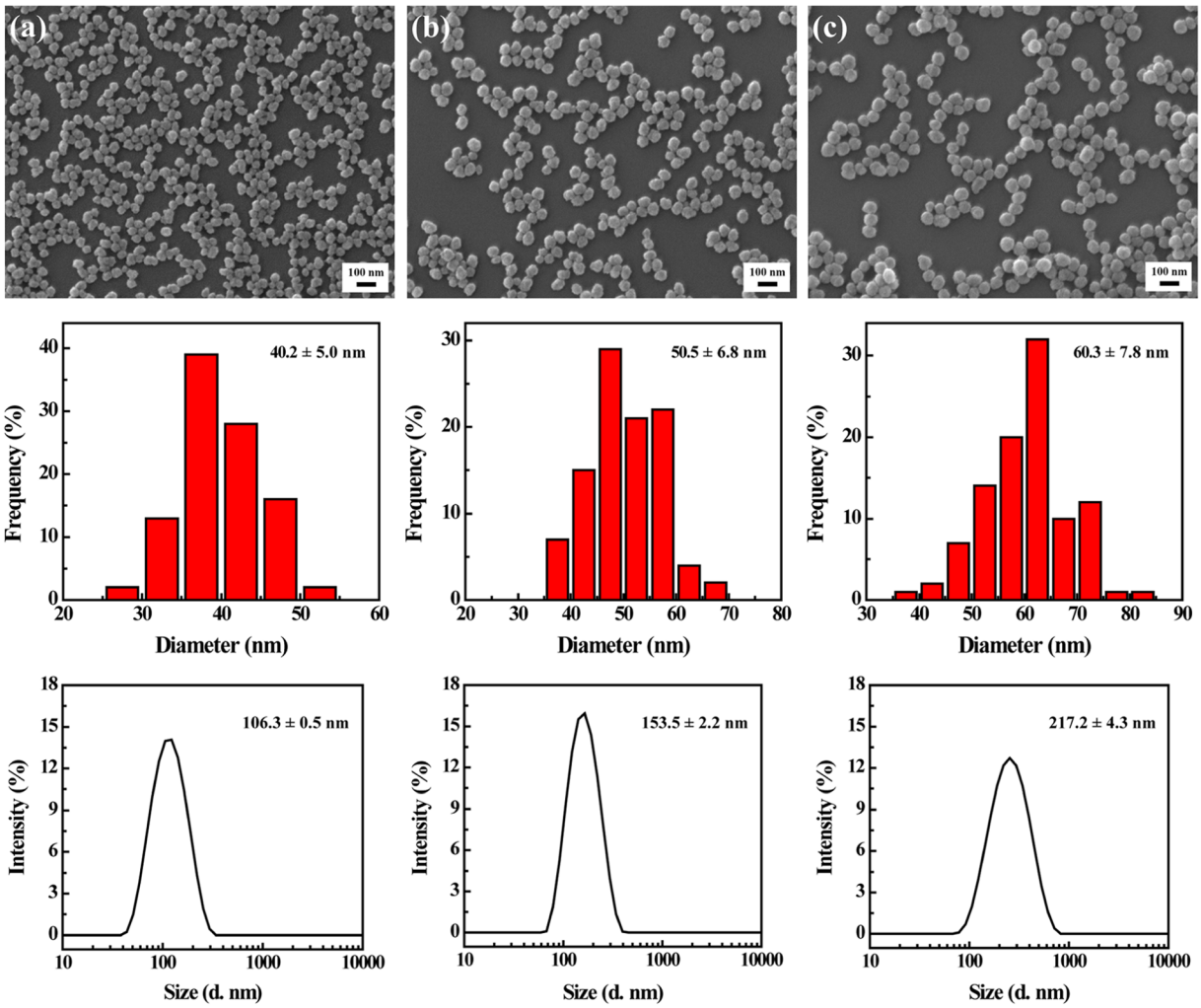

Fig. 1 FE-SEM images (top row), size distributions (middle row), and hydrodynamic sizes of the formed PPy NPs with a size approximate 40 (**a**), 50 (**b**), and 60 nm (**c**)

viabilities were measured using the abovementioned CCK-8 assay.

The photothermal therapy effect of PPy NPs on HeLa cells was further confirmed using a calcein AM staining method, in which the green fluorescence from calcein AM indicates live cells. In this case, approximately 1.5×10^5 HeLa cells were seeded into a 24-well plate. After 24-h incubation, the medium containing P50 NPs of different concentrations was added into the wells. After 12-h incubation, the medium was removed and then the cells were irradiated with an 808-nm laser at a power density of 1.0 W/cm^2 for 10 min. After washing with PBS buffer, the cells were stained with calcein AM solution for 15 min. After staining, the cells were washed with PBS buffer again and the images were captured using an inverted fluorescence microscope.

Results and discussion

PPy NPs were prepared using a facile aqueous dispersion polymerization method. In this procedure, PVA was employed as a stabilizer and $FeCl_3$ played the role of an oxidizing agent to initiate the polymerization of pyrrole

Table 1 The polydispersities and zeta potentials of the formed PPy NPs

Sample	Polydispersity	Zeta potential (mV)
P40	0.143 ± 0.012	13.7 ± 0.4
P50	0.205 ± 0.019	13.9 ± 0.5
P60	0.191 ± 0.017	12.6 ± 0.3
P50 after laser irradiation	0.183 ± 0.020	14.4 ± 0.3

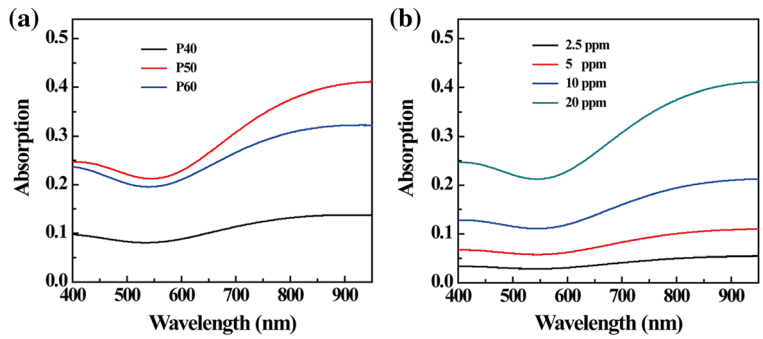

Fig. 2 UV-vis spectra of the formed PPy NPs at the same concentration (**a**) and P50 NPs in aqueous solution with various concentrations (**b**)

monomer. Their sizes could be tuned simply by varying the PVA concentration. Their sizes and morphologies were characterized using FE-SEM. It can be seen from Fig. 1 (top row) that all the PPy NPs were uniformly spherical in shape showing narrow size distributions. Their mean diameters were calculated to be 40.2, 50.5, and 60.3 nm (Fig. 1, middle row); hence, the corresponding PPy NPs were denoted as P40, P50, and P60 NPs, respectively. The hydrodynamic sizes measured by DLS (Fig. 1, bottom row, and Table 1) further confirmed their narrow size distributions, which showed single peaks with narrow width. It is noticed that the measured hydrodynamic sizes were much larger than that measured by FE-SEM. This can be attributed to the fact that DLS measures the size of NP clusters in aqueous solutions that may consist of many NPs containing hydration shell, while FE-SEM just measures single NP in dry state (Liu et al. 2014). All PPy NPs showed low polydispersity and similar positive surface potential regardless of their sizes (Table 1). Taking P50 NPs for example (Table 2), they showed similar hydrodynamic size and polydispersity in all studied conditions. The zeta potential decreased to negative value and nearly neutral value when dispersed in water containing 10% FBS and pH 6.5/pH 7.4 buffers, which may be caused by the absorption of proteins or inorganic salts onto the surface of the NPs. These data indicated that the formed NPs were stable in these studied conditions (Wang et al. 2015). The optical properties of PPy NPs were studied by UV-vis spectroscopy (Fig. 2). All the PPy NPs showed absorption in the NIR region, which is the characteristic of the bipolaronic metallic state of doped polypyrrole (Zha et al. 2013b). Importantly, the size displayed obvious effect on their absorption spectra. P50 NPs showed most obvious NIR absorption compared to P40 and P60 NPs at the same concentration. In addition, the absorption was concentration-dependent, increasing with the PPy concentration. The absorption in the NIR range of P50 NPs became obvious at the concentration of 20 ppm.

The size effect on photoacoustic imaging ability of PPy NPs was investigated in vitro. Using a laser pulse of 704 nm, the formed PPy NPs with different sizes all generated obvious red PA signals (Fig. 3a, inset). Under the same test parameters, P50 NPs showed the brightest PA signal compared to P40 and P60 NPs. Quantitative data analysis further proved their best PA imaging ability (Fig. 3a). The tendency of the obtained PA imaging performance was in consistence with their corresponding absorption in the NIR range (Fig. 2a). This indicates that the adsorption intensity of NPs in the NIR range is a key parameter for selecting PA imaging contrast agent. P50 NPs, which showed the strongest PA signal, were selected for further study. The PA signals of P50 NPs were enhanced with their concentrations, showing brighter images. Their corresponding PA signals increased linearly with the PPy concentration (Fig. 3b).

Table 2 The hydrodynamic sizes, polydispersities, and zeta potentials of P50 NPs in kinds of solvents

Solvent	Hydrodynamic size (nm)	Polydispersity	Zeta potential (mV)
Water	153.5 ± 2.2	0.205 ± 0.019	13.9 ± 0.5
Water plus 10% FBS	139.7 ± 2.7	0.242 ± 0.018	− 8.2 ± 0.5
Buffer (pH 6.5)	142.1 ± 4.1	0.141 ± 0.032	1.4 ± 0.1
Buffer (pH 7.4)	145.1 ± 4.6	0.163 ± 0.051	0.5 ± 0.0

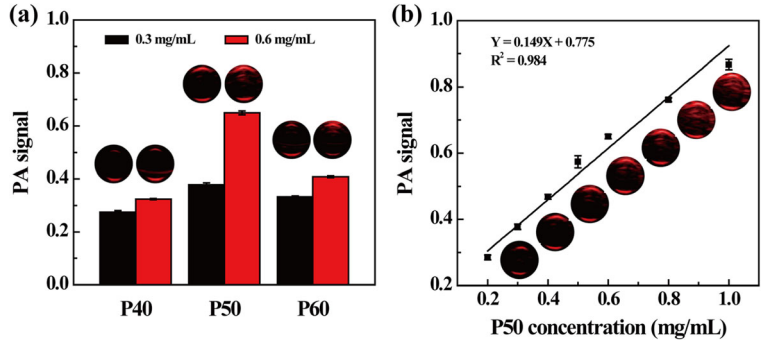

Fig. 3 PA signals and images of **a** PPy NPs with different sizes at the same concentration of 0.3 and 0.6 mg/mL, and **b** P50 NPs in the concentration range of 0.2 to 1.0 mg/mL

Then the effect of particle size on the photothermal properties of PPy NPs was studied under irradiation of an 808-nm laser at a power density of 1.0 W/cm^2 (Fig. 4a–c). At the same concentration, 10 or 20 ppm, P50 NPs showed highest temperature evaluation. For example, P50 NPs of 20 ppm generated a 25.2 °C temperature evaluation after 600 s laser irradiation, while it was only 13.4 and 20.6 °C for P40 and P60 NPs, respectively. This could be induced by their different ability of NIR absorption, which was consistent with the PA imaging data. For P50 NPs, their photothermal performance was improved by increasing the NP concentration (Fig. 4d, e).

The photothermal stability is an important parameter to evaluate photothermal agents. The photothermal reproducibility of P50 NPs was studied by irradiating them with five laser on (10 min)-off (20 min) cycles (Fig. 5a). The temperature evaluation remained almost the same during the 5 cycles, indicating that there was no photo-bleaching. After 5-cycle irradiation, their optical property and hydrodynamic size remained similar

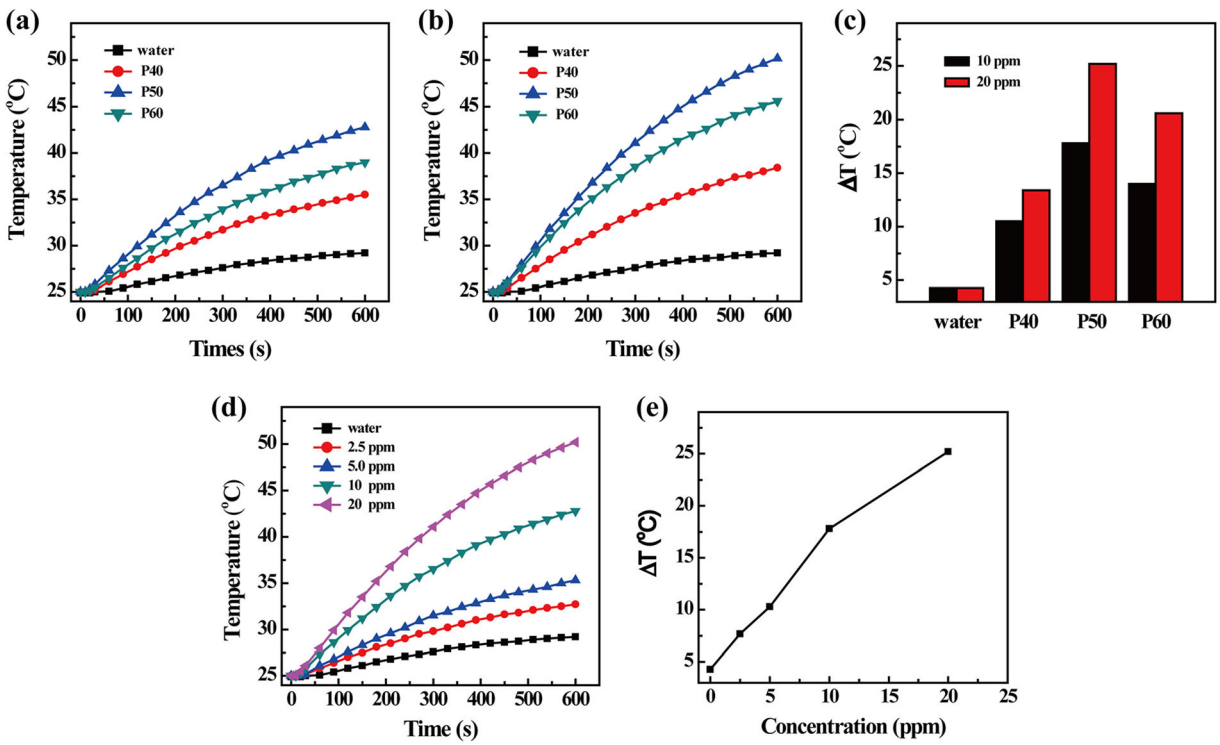

Fig. 4 Temperature curves of PPy NP aqueous solutions under 808-nm laser irradiation at a power density of 1.0 W/cm^2. PPy NPs with different sizes at a concentration of 10 (**a**) and 20 ppm (**b**) and their corresponding temperature increases (**c**). P50 NPs with different concentrations (**d**) and their corresponding temperature increases (**e**)

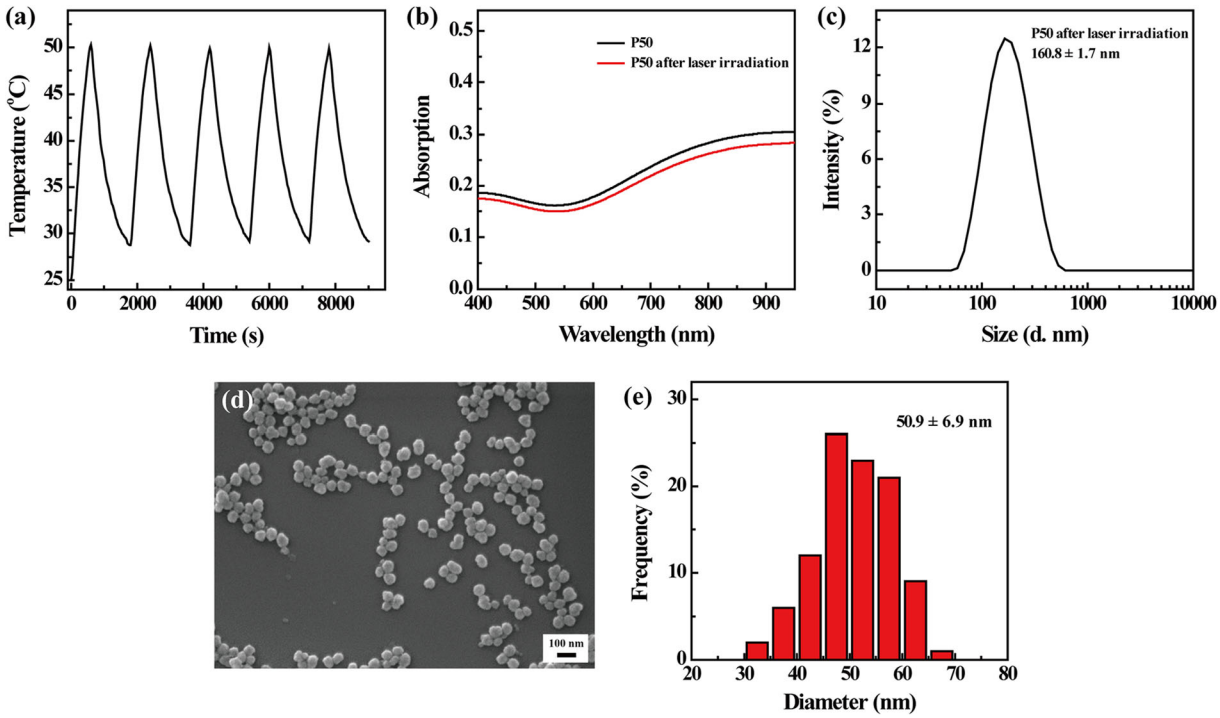

Fig. 5 **a** Temperature curve of 20 ppm P50 NP aqueous solution during five laser on-off cycles under 808-nm laser irradiation at a power density of 1.0 W/cm^2. **b** UV-vis spectra of the P50 NPs before and after laser irradiation. Hydrodynamic size (**c**), FE-SEM image (**d**), and size distribution (**e**) of P50 NPs after laser irradiation

to the as-prepared NPs (Fig. 5b, c). In addition, the P50 NPs after laser irradiation displayed similar morphology and size distribution to the as-prepared NPs (Fig. 5d, e). These data indicated that the formed PPy NPs had desirable photothermal stability compared to conventional small molecular organic photothermal agents (Dong et al. 2016).

For potential biomedical application, it is essential to evaluate the in vitro cytocompatibility of the nanomaterials. HeLa cells were chosen to evaluate the cytotoxicity of the formed PPy NPs using a well-established CCK-8 method. Compared to the well-studied 24- and 48-h incubation times, few studies paid attention to the shorter incubation time to investigate the acute toxicity of the nanoparticles (Wang et al. 2013). Herein, the relative viabilities of HeLa cells co-incubated with P50 NPs for different times were studied. As shown in Fig. 6a, the cell viability decreased obviously when co-incubated with P50 NPs of 100–300 ppm for 2 h, indicating the acute cytotoxicity of PPy NPs. When the incubation time was prolonged to 6 h, the cell viability was not affected under lower concentration; however, the cytotoxicity became obvious when the concentration was above 200 ppm. The cell viability was further improved when the incubation time increased to 12 h. In 24 h, the cell viability under all concentrations was above 90% when compared to the blank control. When using L929 cells for testing, similar results were obtained (Fig. 6b), indicating the cellular uptake of P50 NPs was caused by non-specific charge interactions. Further surface modification of targeting ligands is needed to enhance their potentiality in cancer theranostic applications. The higher cell viability after 12 h co-incubation may be caused by the strong proliferation abilities of HeLa cells and L929 cells, which could help the recovery of their viabilities. The desirable cytocompatibility of PPy NPs in 24-h incubation was further confirmed by the cell morphology observation study (Fig. 6c–g). When incubated with 150–300 ppm P50 NPs for 24 h, the cell morphology did not change obviously compared with the cells treated with PBS buffer. These data suggested that the corresponding acute cytotoxicity needs to be considered when using bare PPy NPs for biomedical applications. The cellular uptake and localization of P50 NPs was observed using a confocal laser scanning microscopy (Fig. 7), which exhibited the localization of cell nuclei (Hoechst

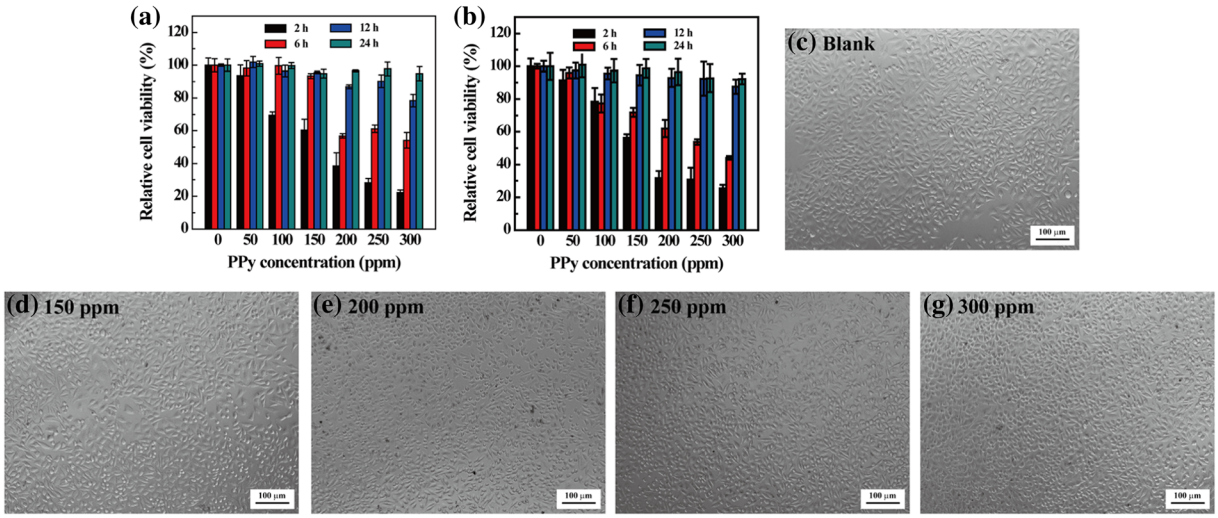

Fig. 6 Relative viability of HeLa cells (**a**) and L929 cells (**b**) co-incubated with P50 NPs under different concentrations and incubation times measured by CCK-8 assay. **c**–**g** Morphology images of the HeLa cells co-incubated with P50 NPs under different concentrations for 24 h

33342) and the 5-FAM-labeled P50 NPs. The imaging results showed that P50 NPs were located around the cell nuclei, indicating their localization in cytoplasm.

The photothermal therapy ability of P50 NPs against HeLa cells was investigated using CCK-8 method (Fig. 8a). After the HeLa cells were co-

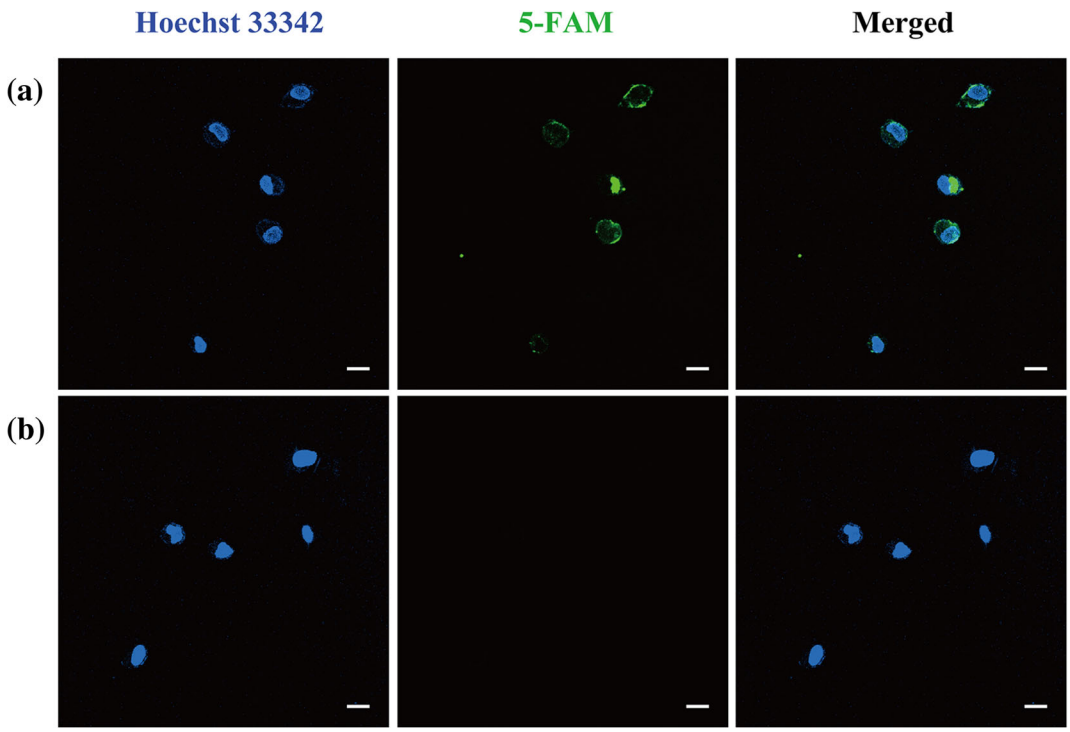

Fig. 7 Confocal fluorescence images of HeLa cells after 6-h co-incubation with fluorescence-labeled P50 NPs (**a**). **b** The corresponding control without NP treatment. The fluorescence of Hoechst 33342 and 5-FAM were pseudo-labeled with blue and green, respectively. Scale bars: 20 μm

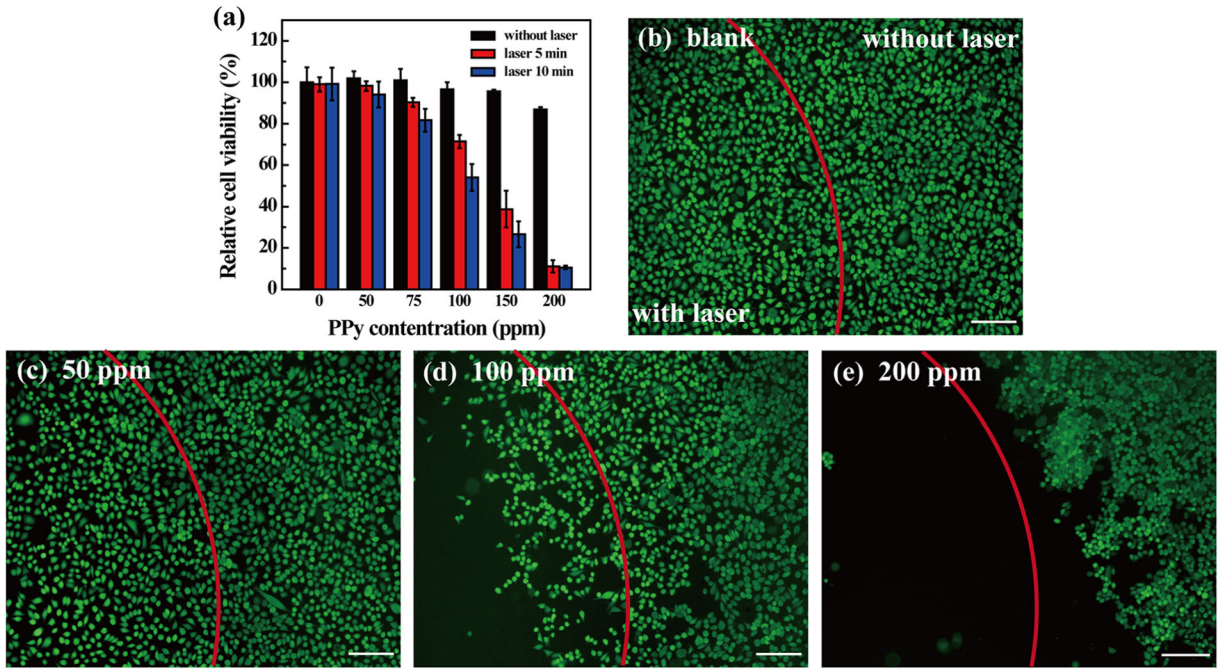

Fig. 8 **a** Relative viability of HeLa cells co-incubated with P50 NPs with different concentrations for 12 h and then irradiated using an 808-nm laser (1.0 W/cm^2) for 5 or 10 min. **b–e** Fluorescence images of HeLa cells co-incubated with P50 NPs with different concentrations for 12 h and irradiated using the same laser for 10 min. The green fluorescence of calcein AM staining indicates live cells

incubated with P50 NPs for 12 h at the concentration range from 0 to 200 ppm, the cell viability remained above 85% without laser irradiation. However, after treatment with P50 NPs and laser irradiation (808 nm, 1.0 W/cm^2, 5 or 10 min), the relative cell viabilities decreased remarkably as the concentration increased. At lower concentrations of 0–75 ppm, over 80% of HeLa cells remained alive with 5 or 10 min NIR laser irradiation, showing no obvious photothermal effect. In contrast, the cell viability decreased evidently under laser irradiation at higher concentration range of 100–200 ppm. In particular, approximately 10% of cells remained viable when co-incubated with 200 ppm P50 NPs under laser irradiation for 5 or 10 min, indicating a significant photothermal ablation effect on HeLa cells. This was further confirmed by calcein AM staining, in which the green fluorescence indicates the viability of cells. After 12-h co-incubation and 10-min laser irradiation, the green fluorescence of cells in the laser irradiation area became weaker under the higher concentration (Fig. 8b–e). This was consistent with the cell viability data measured by CCK-8 assay.

Conclusions

In summary, PPy NPs with size range of 40–60 nm were prepared through a facile aqueous dispersion polymerization method. The formed PPy NPs were uniformly spherical in shape with narrow size distribution. The size of PPy NPs showed an evident effect on their NIR absorption and then affected their photoacoustic imaging property and photothermal conversion ability. The P50 NPs displayed optimal potentiality among the three formed PPy NPs. The photo-stability of P50 NPs was proved to be desirable. CCK-8 assays showed that PPy NPs exhibited obvious acute cytotoxicity, which needs to be considered in further preclinical studies in vivo. Confocal images showed that P50 NPs could be internalized into the cytoplasm by HeLa cells after 6-h co-incubation. The photothermal therapy ability of P50 NPs against HeLa cells was proved to be effective under studied condition. This study provided a rational design of a multifunctional nanoplatform based on PPy NPs for photoacoustic imaging and photothermal therapy, and the results indicated the prominent potential of this system that could be applied for cancer diagnosis and therapy.

Acknowledgements This work was supported by the start-up grant from Southwest University (SWU116027, SWU115059), the Fundamental Research Funds for Central Universities from Southwest University (XDJK2016C153), the Chongqing Research Program of Basic Research and Frontier Technology (cstc2017jcyjAX0066), and the National Natural Science Foundation of China (81401503, 31671037, 51703184). Y.C. gratefully acknowledges the funding support of China Postdoctoral Science Foundation funded projects (2015T80963, 2016M590869) and Chongqing Postdoctoral Science Foundation funded project (Xm2015089).

Compliance with ethical standards

Conflict of interest The authors declare that they have no conflict of interests.

References

Ahmad R, Fu J, He N, Li S (2016) Advanced gold nanomaterials for photothermal therapy of cancer. J Nanosci Nanotechno 16(1):67–80

Cai H, Li K, Shen M, Wen S, Luo Y, Peng C, Zhang G, Shi X (2012) Facile assembly of Fe3O4@Au nanocomposite particles for dual mode magnetic resonance and computed tomography imaging applications. J Mater Chem 22(30):15110

Chen M, Fang X, Tang S, Zheng N (2012) Polypyrrole nanoparticles for high-performance in vivo near-infrared photothermal cancer therapy. Chem Commun 48(71):8934–8936

Chen D, Wang C, Nie X, Li S, Li R, Guan M, Liu Z, Chen C, Wang C, Shu C, Wan L (2014a) Photoacoustic imaging guided near-infrared photothermal therapy using highly water-dispersible single-walled carbon nanohorns as theranostic agents. Adv Funct Mater 24(42):6621–6628

Chen M, Tang S, Guo Z, Wang X, Mo S, Huang X, Liu G, Zheng N (2014b) Core-shell Pd@Au nanoplates as theranostic agents for in-vivo photoacoustic imaging, CT imaging, and photothermal therapy. Adv Mater 26(48):8210–8216

Cheng L, Liu J, Gu X, Gong H, Shi X, Liu T, Wang C, Wang X, Liu G, Xing H, Bu W, Sun B, Liu Z (2014) PEGylated WS2 nanosheets as a multifunctional theranostic agent for in vivo dual-modal CT/photoacoustic imaging guided photothermal therapy. Adv Mater 26(12):1886–1893

Deng H, Dai F, Ma G, Zhang X (2015) Theranostic gold nanomicelles made from biocompatible comb-like polymers for thermochemotherapy and multifunctional imaging with rapid clearance. Adv Mater 27(24):3645–3653

Dong Z, Gong H, Gao M, Zhu W, Sun X, Feng L, Fu T, Li Y, Liu Z (2016) Polydopamine nanoparticles as a versatile molecular loading platform to enable imaging-guided cancer combination therapy. Theranostics 6(7):1031–1042

Fan Q, Cheng K, Yang Z, Zhang R, Yang M, Hu X, Ma X, Bu L, Lu X, Xiong X, Huang W, Zhao H, Cheng Z (2015) Perylene-diimide-based nanoparticles as highly efficient photoacoustic agents for deep brain tumor imaging in living mice. Adv Mater 27(5):843–847

Guha S, Shaw GK, Mitcham TM, Bouchard RR, Smith BD (2016) Croconaine rotaxane for acid activated photothermal heating and ratiometric photoacoustic imaging of acidic pH. Chem Commun 52(1):120–123

Hong J-Y, Yoon H, Jang J (2010) Kinetic study of the formation of polypyrrole nanoparticles in water-soluble polymer/metal cation systems: a light-scattering analysis. Small 6(5):679–686

Hu D, Liu C, Song L, Cui H, Gao G, Liu P, Sheng Z, Cai L (2016a) Indocyanine green-loaded polydopamine-iron ions coordination nanoparticles for photoacoustic/magnetic resonance dual-modal imaging-guided cancer photothermal therapy. Nano 8(39):17150–17158

Hu D, Zhang J, Gao G, Sheng Z, Cui H, Cai L (2016b) Indocyanine green-loaded polydopamine-reduced graphene oxide nanocomposites with amplifying photoacoustic and photothermal effects for cancer theranostics. Theranostics 6(7):1043–1052

Huang Y, He S, Cao W, Cai K, Liang XJ (2012) Biomedical nanomaterials for imaging-guided cancer therapy. Nano 4(20):6135–6149

Huang P, Lin J, Li W, Rong P, Wang Z, Wang S, Wang X, Sun X, Aronova M, Niu G (2013) Biodegradable gold nanovesicles with an ultrastrong plasmonic coupling effect for photoacoustic imaging and photothermal therapy. Angew Chem Int Edit 125(52):14208–14214

Jin Y, Li Y, Ma X, Zha Z, Shi L, Tian J, Dai Z (2014) Encapsulating tantalum oxide into polypyrrole nanoparticles for X-ray CT/photoacoustic bimodal imaging-guided photothermal ablation of cancer. Biomaterials 35(22):5795–5804

Li Y, Jiang C, Zhang D, Wang Y, Ren X, Ai K, Chen X, Lu L (2017) Targeted polydopamine nanoparticles enable photoacoustic imaging guided chemo-photothermal synergistic therapy of tumor. Acta Biomater 47:124–134

Liang X, Li Y, Li X, Jing L, Deng Z, Yue X, Li C, Dai Z (2015) PEGylated polypyrrole nanoparticles conjugating gadolinium chelates for dual-modal MRI/photoacoustic imaging guided photothermal therapy of cancer. Adv Funct Mater 25(9):1451–1462

Liang X, Fang L, Li X, Zhang X, Wang F (2017) Activatable near infrared dye conjugated hyaluronic acid based nanoparticles as a targeted theranostic agent for enhanced fluorescence/CT/photoacoustic imaging guided photothermal therapy. Biomaterials 132:72–84

Liao J, Qi T, Chu B, Peng J, Luo F, Qian Z (2014) Multifunctional nanostructured materials for multimodal cancer imaging and therapy. J Nanosci Nanotechno 14(1):175–189

Liu H, Wang H, Xu Y, Shen M, Zhao J, Zhang G, Shi X (2014) Synthesis of PEGylated low generation dendrimer-entrapped gold nanoparticles for CT imaging applications. Nano 6:4521–4526

Liu F, He X, Lei Z, Liu L, Zhang J, You H, Zhang H, Wang Z (2015) Facile preparation of doxorubicin-loaded upconversion@polydopamine nanoplatforms for simultaneous in vivo multimodality imaging and chemophotothermal synergistic therapy. Adv Healthcare Mater 4(4):559–568

Opoku-Damoah Y, Wang R, Zhou J, Ding Y (2016) Versatile nanosystem-based cancer theranostics: design inspiration and predetermined routing. Theranostics 6(7):986–1003

Song KH, Stein EW, Margenthaler JA, Wang LV (2008) Noninvasive photoacoustic identification of sentinel lymph

nodes containing methylene blue in vivo in a rat model. J Biomed Opt 13(5):054033

Song G, Shen J, Jiang F, Hu R, Li W, An L, Zou R, Chen Z, Qin Z, Hu J (2014) Hydrophilic molybdenum oxide nanomaterials with controlled morphology and strong plasmonic absorption for photothermal ablation of cancer cells. ACS Appl Mater Inter 6(6):3915–3922

Song X, Chen Q, Liu Z (2015) Recent advances in the development of organic photothermal nano-agents. Nano Res 8(2): 340–354

Wang X, Pang Y, Ku G, Xie X, Stoica G, Wang LV (2003) Noninvasive laser-induced photoacoustic tomography for structural and functional in vivo imaging of the brain. Nat Biotechnol 21(7):803–806

Wang K, Gao Z, Gao G, Wo Y, Wang Y, Shen G, Cui D (2013) Systematic safety evaluation on photoluminescent carbon dots. Nanoscale Res Lett 8(1):122

Wang L, Lin X, Wang J, Hu Z, Ji Y, Hou S, Zhao Y, Wu X, Chen C (2014a) Novel insights into combating cancer chemotherapy resistance using a plasmonic nanocarrier: enhancing drug sensitiveness and accumulation simultaneously with localized mild photothermal stimulus of femtosecond pulsed laser. Adv Funct Mater 24(27):4229–4239

Wang Q, Wang J, Lv G, Wang F, Zhou X, Hu J, Wang Q (2014b) Facile synthesis of hydrophilic polypyrrole nanoparticles for photothermal cancer therapy. J Mater Sci 49(9):3484–3490

Wang L, Sun Q, Wang X, Wen T, Yin J, Wang P, Bai R, Zhang X, Zhang L, Lu A, Chen C (2015) Using hollow carbon nanospheres as a light-induced free radical generator to overcome chemotherapy resistance. J Am Chem Soc 137(5):1947–1955

Wang S, Zhao J, Yang H, Wu C, Hu F, Chang H, Li G, Ma D, Zou D, Huang M (2017) Bottom-up synthesis of WS2 nanosheets with synchronous surface modification for imaging guided tumor regression. Acta Biomater 58:442–454

Wen S, Li K, Cai H, Chen Q, Shen M, Huang Y, Peng C, Hou W, Zhu M, Zhang G, Shi X (2013) Multifunctional dendrimer-entrapped gold nanoparticles for dual mode CT/MR imaging applications. Biomaterials 34(5):1570–1580

Yang K, Feng L, Shi X, Liu Z (2013) Nano-graphene in biomedicine: theranostic applications. Chem Soc Rev 42(2):530–547

Yang Z, Ren J, Ye Z, Zhu W, Xiao L, Zhang L, He Q, Xu Z, Xu H (2017) Bio-inspired synthesis of PEGylated polypyrrole@polydopamine nanocomposites as theranostic agents for T1-weighted MR imaging guided photothermal therapy. J Mater Chem B 5(5):1108–1116

Zha Z, Deng Z, Li Y, Li C, Wang J, Wang S, Qu E, Dai Z (2013a) Biocompatible polypyrrole nanoparticles as a novel organic photoacoustic contrast agent for deep tissue imaging. Nano 5(10):4462–4467

Zha Z, Yue X, Ren Q, Dai Z (2013b) Uniform polypyrrole nanoparticles with high photothermal conversion efficiency for photothermal ablation of cancer cells. Adv Mater 25(5):777–782

Zha Z, Zhang S, Deng Z, Li Y, Li C, Dai Z (2013c) Enzyme-responsive copper sulphide nanoparticles for combined photoacoustic imaging, tumor-selective chemotherapy and photothermal therapy. Chem Commun 49(33):3455–3457

Zhang L, Su H, Cai J, Cheng D, Ma Y, Zhang J, Zhou C, Liu S, Shi H, Zhang Y, Zhang C (2016) A multifunctional platform for tumor angiogenesis-targeted chemo-thermal therapy using polydopamine-coated gold nanorods. ACS Nano 10(11): 10404–10417